

# Impact of Electrical Current on Single GaAs Nanowire Structure

Danial Bahrami, Ali AlHassan, Arman Davtyan, Ren Zhe, Taseer Anjum, Jesús Herranz, Lutz Geelhaar, Dmitri V. Novikov, Rainer Timm, and Ullrich Pietsch\*

The impact of electrical current on the structure of single free-standing Be-doped GaAs nanowires grown on a Si 111 substrate is investigated. Single nanowires have been structurally analyzed by X-ray nanodiffraction using synchrotron radiation before and after the application of an electrical current. The conductivity measurements on single nanowires in their as-grown geometry have been realized via W-probes installed inside a dual-beam focused ion beam/scanning electron microscopy chamber. Comparing reciprocal space maps of the 111 Bragg reflection, extracted perpendicular to the nanowire growth axis before and after the conductivity measurement, the structural impact of the electrical current is evidenced, including deformation of the hexagonal nanowire cross section, tilting, and bending with respect to the substrate normal. For electrical current densities below  $30 \text{ A mm}^{-2}$ , the induced changes in the reciprocal space maps are negligible. However, for a current density of  $347 \text{ A mm}^{-2}$ , the diffraction pattern is completely distorted. The mean cross section of the illuminated nanowire volume is reconstructed from the reciprocal space maps before and after the application of electrical current. Interestingly, the elongation of two pairs of opposing side facets accompanied by shrinkage of the third pair of facets is found. The variations in the nanowire diameter, as well as their tilt and bending, are confirmed by scanning electron microscopy. To explain these findings, material melting due to Joule heating during voltage/current application accompanied by anisotropic deformations induced by the W-probe is suggested.

applications of semiconductor NWs in electronics,<sup>[1–4]</sup> photonics,<sup>[5]</sup> and optoelectronics<sup>[6]</sup> are strongly affected by their structural properties such as lattice strain<sup>[7]</sup> and phase purity.<sup>[8]</sup> For profound understanding of the impact of structure on future electronic device performance, it is important to study the correlation between structural and electrical properties. In a previous study, we were able to demonstrate that the electrical resistance of single GaAs NWs changes with the number of intrinsic interfaces along the NW growth axis.<sup>[9]</sup> Since the number of intrinsic axial interphases, such as interfaces between wurtzite and zincblende or stacking faults, differs among NWs grown on same substrate, each single NW implemented in a nanodevice may exhibit a particular performance depending on real structure. A real nanodevice shows various axial or radial interfaces and local doping. Moreover, each nanooptic or nanoelectronic device is running by applying a certain electrical current. Since the potential barrier to introduce a stacking fault is very small even a small electrical current might induce a change on the device performance. Therefore, in this report, we systematically investigated the impact of different amplitudes of electrical current passing through single GaAs NWs on their structural properties. It is supposed that above a certain threshold of current changes in the NW real structure and therefore changes in device performance cannot be excluded. Due to the

## 1. Introduction

The characterization and control of the physical properties of semiconductor nanowires (NWs) are fundamental for their implementation into future devices. For example, the


tematically investigated the impact of different amplitudes of electrical current passing through single GaAs NWs on their structural properties. It is supposed that above a certain threshold of current changes in the NW real structure and therefore changes in device performance cannot be excluded. Due to the

Dr. D. Bahrami, Dr. A. AlHassan, Dr. A. Davtyan, Dr. T. Anjum, Prof. U. Pietsch  
Physik Department  
Naturwissenschaftlich-Technische Fakultät der Universität Siegen  
Siegen 57068, Germany  
E-mail: pietsch@physik.uni-siegen.de

Dr. R. Zhe, Prof. R. Timm  
Department of Physics and NanoLund  
Lund University  
Lund 221 00, Sweden

Dr. J. Herranz, Dr. L. Geelhaar  
Paul-Drude-Institut für Festkörperelektronik  
Leibniz-Institut im Forschungsverbund Berlin e.V.  
Hausvogteiplatz 5-7, Berlin 10117, Germany

Dr. D. V. Novikov  
PETRA III  
Deutsches Elektronen-Synchrotron DESY  
Hamburg 22607, Germany

 The ORCID identification number(s) for the author(s) of this article can be found under <https://doi.org/10.1002/pssb.202100056>.

© 2021 The Authors. physica status solidi (b) basic solid state physics published by Wiley-VCH GmbH. This is an open access article under the terms of the Creative Commons Attribution License, which permits use, distribution and reproduction in any medium, provided the original work is properly cited.

DOI: 10.1002/pssb.202100056

small NW diameter, even absolute currents in the microampere range result in very high current densities which increase the temperature in the NW material through Joule heating,<sup>[10,11]</sup> possibly reaching temperatures where structural NW properties get affected. The heat  $Q$  dissipated in the NW over a time  $t$  through Joule heating depends on the current  $I$  and the NW resistance  $R$  according to  $Q = I^2 R t$ . Since heat transport in the NW is very fast and the substrate can be considered as an almost infinite heat sink due to the small volume and density of the NWs, equilibrium conditions will be reached within a few nanoseconds,<sup>[12]</sup> as will be discussed in more detail in the following section.

The structural characterization of single NWs is mostly performed by transmission electron microscopy (TEM)-based techniques, i.e., high-resolution TEM,<sup>[13]</sup> scanning TEM,<sup>[14]</sup> and energy-dispersive spectroscopy.<sup>[15]</sup> Although atomic resolution can be achieved using TEM, the structural characterization of NWs with large diameters using this technique requires an arduous sample preparation process. Furthermore, performing TEM on specific NWs that are 3–4  $\mu\text{m}$  long is rather challenging. Instead, nano X-ray diffraction (nXRD) has been used as a complementary and preparation-free technique that permits probing several preselected single NWs grown on the same substrate in their as-grown geometry.<sup>[16,17]</sup> The nXRD was used as an alternative technique to extract the structural information from single NWs before and after conductivity measurements. As shown recently, nXRD becomes destructive if the radiation dose exceeds a certain threshold.<sup>[18]</sup> However, the nXRD studies shown in this article have been performed at doses much below this threshold.

Conductivity measurements on NWs are usually realized in the geometry of a field-effect transistor (FET). In this case, the NWs are detached from their original positions on the substrate and are laterally deposited onto an insulating substrate. Then, the NW is contacted with 2 or 4 metallic electrodes which are defined by electron beam lithography (EBL).<sup>[19,20]</sup> However, there are important constraints in using this geometry: 1) the collected data from a broken NW are not compatible to device application requesting free-standing NWs.<sup>[21,22]</sup> 2) The EBL processing can cause perturbation of the NW surface due to impact of chemicals during the photolithography process. 3) The measured current–voltage ( $I$ – $V$ ) characteristics in two-point terminal geometry are partially governed by the contact instead of the NW itself.<sup>[23,24]</sup> A rather uncommon, but in several aspects superior approach is to probe NWs in their as-grown geometry on the substrate using a sharp metallic probe with precisely controlled position.<sup>[10,25–27]</sup> In this approach, the NW is suitable for further characterization by different experimental techniques and avoids any damage which can be induced during the removal of the NW from the substrate.

The aim of this experiment was to compare reciprocal space maps (RSMs) acquired from a few selected NWs before and after applying an electrical voltage, studying current-induced structural changes. Structural information of individual GaAs NWs was revealed by nXRD using focused synchrotron radiation. An electrical bias was applied and  $I$ – $V$  characterization was performed on the same NWs in their as-grown geometry using a metallic W-probe installed inside a dual-focused ion beam (FIB)/scanning electron microscopy (SEM) system. We report on significant and unexpected changes in the NW morphology, namely, thickness variation between opposing side facets which

results in modifying the hexagonal symmetry of the NW cross section as a function of electrical current density applied through the NW.

## 2. Experimental Section

For this study, we used Be-doped GaAs 111 oriented NWs grown by self-catalyzed molecular beam epitaxy (MBE)<sup>[28]</sup> on a highly p-doped Si 111 substrate covered with a 20 nm thick oxide layer patterned by EBL. For better mechanical stability during the contacting by the W-probe, the NWs were grown in two steps. First, a Be-doped GaAs NW core was grown via the vapor–liquid–solid mechanism with a height of about 4  $\mu\text{m}$  and about 100 nm diameter with nominal doping concentration of  $10^{19} \text{ cm}^{-3}$ . Then, after the consumption of the Ga droplet, a 50 nm thick Be-doped ( $10^{19} \text{ cm}^{-3}$ ) GaAs homo-shell around the core, a Be-doped GaAs shell was grown via the vapor–solid mechanism to obtain a total nominal diameter of around 200–230 nm. To access the same NWs with the conductive probe and the X-ray beam, holes with a separation of 10  $\mu\text{m}$  were patterned by EBL within the Si oxide layer of the substrate before NW growth. These holes, with diameters around 70 nm, acted as nucleation sites for NW growth. More details about the growth parameters and procedure can be found in a previous study.<sup>[29]</sup>

This study was conducted in three progressive phases: During the 1st phase, we recorded RSMs in the vicinity of the GaAs 111 Bragg reflection from single NWs by means of nXRD. In the 2nd phase, electrical biasing and  $I$ – $V$  characterization were performed to the same NWs in their as-grown geometry. The 3rd phase was similar to the first, such that RSMs of the GaAs 111 Bragg reflection were acquired from the same NWs. The experiments in the 1st and 3rd phases were performed at beamline P23 of PETRAIII at DESY using a photon energy of 10 keV under ambient conditions.

### 2.1. X-Ray Diffraction Experiment (Phase I)

The X-ray beam was focused with a Fresnel zone plate down to a focal size of 0.8  $\mu\text{m}$  (vertical)  $\times$  3  $\mu\text{m}$  (horizontal) providing the spatial resolution required inspecting single NWs. To locate the beam at the region of interest on the sample, scanning X-ray diffraction microscopy (SXDM) was performed to produce a real space image of the NW regions.<sup>[30]</sup> To record real space images, first, we set the angle of incidence to the GaAs 111 Bragg reflection. Second, the sample was translated perpendicular and parallel to the beam whereas the scattering signal was collected by a 2D LAMBDA detector. Third, the recorded intensity frames were integrated and then plotted as function of lateral motor positions. The resulting SXDM 2D plot and the SEM image of the investigated region are shown in Figure S1, Supporting Information. Finally, a RSM of the GaAs 111 Bragg reflection was recorded for each individual NW by varying the angle of the incident beam and simultaneously recording 2D detector images of the scattering signal. More details about the procedure to record RSMs can be found in the studies by AlHassan et al., Davtyan et al., and AlHassan et al.<sup>[16–18]</sup>

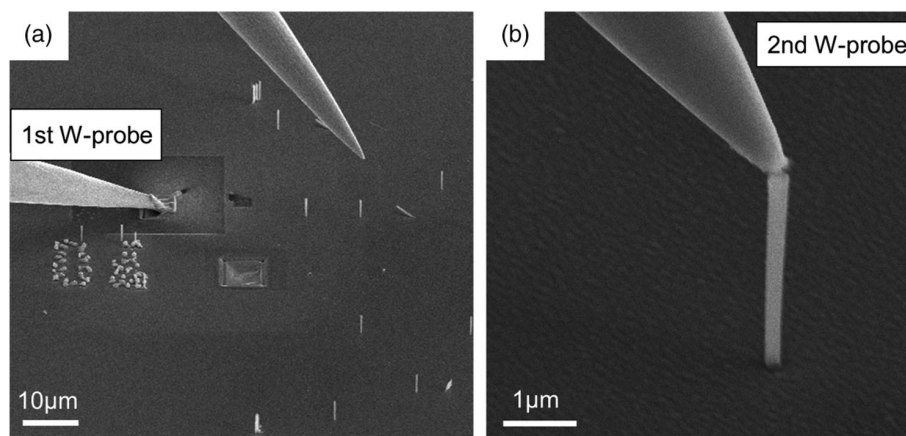


**Figure 1.** Tilted SEM images of the two W-probes on the NW field of interest. a) The first probe is contacting the substrate and b) the second probe is used to contact a single NW.

## 2.2. Application of Electrical Current (Phase II)

The 2nd phase of the study was performed at the home lab directly after the nXRD experiment. The electrical conductivity measurement was performed in a dual-beam FIB/SEM chamber using two W-probes driven by a piezomanipulator (Kleindiek, MM3A-EM). Before the measurements, good ohmic conductance of both probes and of the highly doped Si substrate of the sample had been confirmed by test measurements. One probe was used to contact the substrate and the other one was used to contact the selected NW from top. The Si oxide layer was removed by FIB milling (using a current of 2.8 nA and a voltage of 30 keV) at a distance of 10–20  $\mu\text{m}$  away from the NWs of interest. The depth of milling was 0.5  $\mu\text{m}$  in an area of about  $6 \times 6 \mu\text{m}^2$ . By means of a gas injector system, a  $4 \times 4 \mu\text{m}^2$  Pt layer with a thickness of 1  $\mu\text{m}$  was deposited on this FIB-milled area. The first W-probe was attached to the Pt layer to provide ohmic contact with the substrate (**Figure 1a**) whereas the second probe was brought in contact with the NWs of interest (**Figure 1b**). A voltage was applied to the single NW using a semiconductor analyzer (Keithley 4200-SCS).

First, we wanted to evaluate the critical current which might lead to the melting or breaking of the NW and applied a stepwise ascending voltage to various single GaAs NWs that were not investigated by nXRD before, until critical damage was observed for different NWs (**Figure S2**, Supporting Information). By normalizing the measured critical currents by the NW cross sections as obtained from SEM images, an average critical current density of  $1157 \pm 50 \text{ A mm}^{-2}$  was observed. In the following, current densities in the NWs were kept far below this critical value.

To compare the impact of different current densities on the NW structure, we applied different voltage levels to single NWs which had been investigated by nXRD in phase I, resulting in maximum electrical currents in the range from 0.9 to 15  $\mu\text{A}$  ( $30\text{--}347 \text{ A mm}^{-2}$ ). The  $I$ - $V$  curves of four different NWs labeled by A, B, C, and D are shown in **Figure 2**. The maximum voltages applied to these NWs and the resulting maximum currents were as follows: NW A 0.8 V and 0.9  $\mu\text{A}$ , NW B 8.0 V and 2  $\mu\text{A}$ , NW C 5.1 V and 5  $\mu\text{A}$ , and NW D 8.2 V and 15  $\mu\text{A}$ . Considering the NW

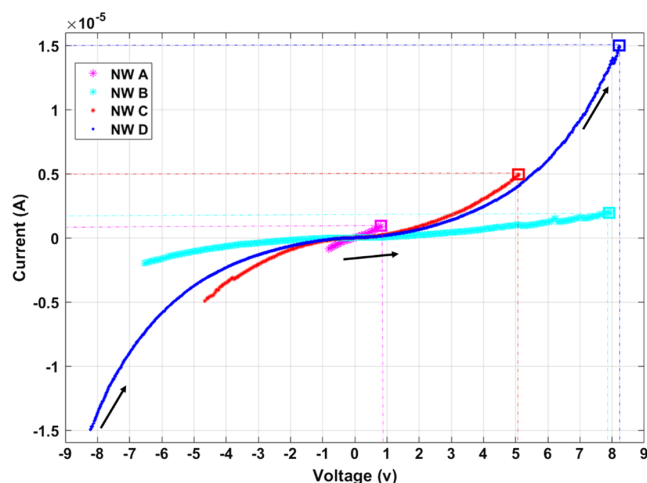


**Figure 2.**  $I$ - $V$  curves of four single NWs. Black arrows indicate the direction of the voltage ramp. Maximum values of the electrical power (applied voltage and obtained current) for each NW are indicated by small squares and dashed lines.

diameter as obtained from SEM images, this corresponded to the following current densities: NW A  $30 \text{ A mm}^{-2}$ , NW B  $55 \text{ A mm}^{-2}$ , NW C  $138 \text{ A mm}^{-2}$ , and NW D  $347 \text{ A mm}^{-2}$ . The maximum electrical power applied to each NW amounted to: NW A 0.72  $\mu\text{W}$ , NW B 16  $\mu\text{W}$ , NW C 26  $\mu\text{W}$ , and NW D 123  $\mu\text{W}$ .

## 2.3. X-Ray Diffraction Experiment (Phase III)

In the 3rd and last phase of the study, we remeasured the same NWs by nXRD after the electrical treatment. For this purpose, the sample was transferred again to P23 beamline at which the experiment was conducted under identical conditions compared to the first XRD experiment (phase I), such that the same beam size and photon flux were used.

### 3. Results and Discussion

#### 3.1. Reciprocal Space Maps

Figure 3 shows results of the three phases of experimental procedures. It shows 2D cuts extracted from the 3D RSM in the plane perpendicular to the NW length axis notified by  $Q_X^{111}$  and  $Q_Y^{111}$ . The 3D RSM of the 111 Bragg reflection is defined by three reciprocal space vectors  $Q_Z^{111}$ ,  $Q_Y^{111}$ , and  $Q_X^{111}$ . Reciprocal space vector  $Q_Z^{111}$  points along the NW growth direction [111] whereas  $Q_X^{111}$  and  $Q_Y^{111}$  are the vectors perpendicular to  $Q_Z^{111}$  and are defined along [1–10] and [11–2], respectively. The top row of images of Figure 3 shows the  $Q_X^{111} - Q_Y^{111}$  RSMs belonging to the four mentioned NWs before conductivity measurement. The bottom row of images shows similar projections measured for the same NWs after electrical contact. In the middle part of Figure 3, the corresponding electrical current density applied to each single NW is mentioned. The respective RSMs provide information about the hexagonal symmetry of the NW cross section, thickness between opposing side facets, and the tilt of the NW with respect to the substrate normal.<sup>[31]</sup> Comparing the diffraction patterns displayed at the top row with the ones at the bottom row of Figure 3, we identify significant changes in symmetry of the diffraction patterns as a function of the electrical current density and power applied to the NWs. The lowest amount was applied to NW A ( $30 \text{ A mm}^{-2}$ ,  $0.72 \mu\text{W}$ ). Comparing the RSMs recorded for NW A before and after the conductivity measurement, only minor changes are visible. The nearly perfect hexagonal symmetry of the diffraction pattern and the identical period of thickness fringes along each of the six truncation rods confirm the hexagonal shape of the NW. After the application of electrical currents, the hexagonal

symmetry of the diffraction pattern is maintained, but the NW is slightly tilted comparing the central peak of the six-sided star to the position of the Si truncation rod, indicated by a red circle in the RSM. The position of the Si truncation rod in  $Q_X^{111} - Q_Y^{111}$  is considered as a reference to compare the NW tilt before and after electrical treatment. The RSMs belonging to NW B and NW C after applying current densities (power) of  $55 \text{ A mm}^{-2}$  ( $16 \mu\text{W}$ ) and  $138 \text{ A mm}^{-2}$  ( $26 \mu\text{W}$ ), respectively, show severe changes. In both maps after electrical treatment, the hexagonal symmetry of the diffraction patterns becomes irregular. In particular, truncation rods of two side facets are not visible anymore. Furthermore, the oscillation fringes belonging to NW C elongate along this direction. Comparing NW B and NW C before and after electrical treatment, the RSMs indicate morphological changes including deformation in the cross section of the wires and tilt. After applying the highest amount of current density ( $347 \text{ A mm}^{-2}$ , or  $123 \mu\text{W}$ ) to NW D, the thickness fringes completely disappear, which is an indication of the full distortion of the hexagonal cross section and its crystallinity.

To have better understanding of the induced structural changes after electrical treatment, we have reconstructed the NWs' cross sections from their respective RSMs.

#### 3.2. Extraction of NW Cross Section from ( $Q_X^{111} - Q_Y^{111}$ ) Projection

The 2D projections in the ( $Q_X^{111}, Q_Y^{111}$ ) plane for the four NWs are shown in the Figure 3. The star-like diffraction patterns are formed of six truncation rods with spaced maxima and minima, which represent the Fourier transformation of the NW hexagonal cross section such that each pair of opposite truncation rods in reciprocal space is perpendicular to a pair of opposite side facets

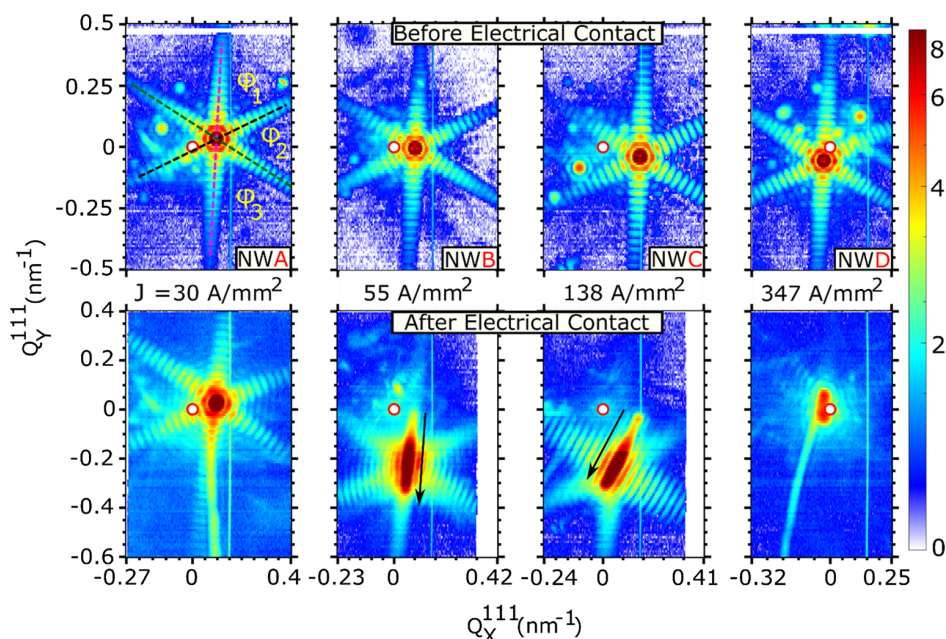


**Figure 3.**  $Q_X^{111} - Q_Y^{111}$  projections of 3D RSMs of the four NWs before and after electrical treatment. The red circle in each map belongs to the Si truncation rod used as a reference in RSM. Black arrows in the RSM of NW B and NW C indicate the tilt direction. The midpart numbers correspond to the current density. (The maximum electrical power: NW A:  $0.72 \mu\text{W}$ , NW B:  $16 \mu\text{W}$ , NW C:  $26 \mu\text{W}$ , and NW D:  $123 \mu\text{W}$ .)

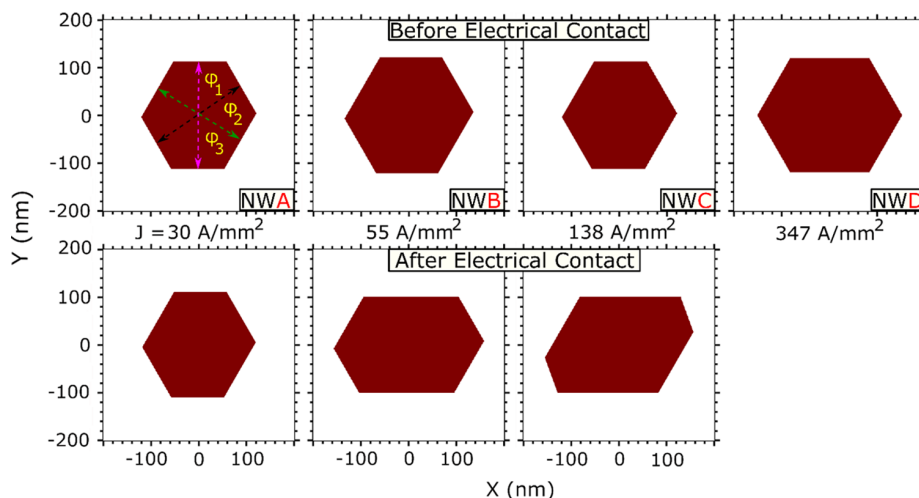


**Figure 4.** Reconstructed cross sections of the NWs calculated from RSM before and after applying electrical current. The midpart numbers corresponded to current density. (The maximum electrical power: NW A: 0.72  $\mu$ W, NW B: 16  $\mu$ W, NW C: 26  $\mu$ W, and NW D: 123  $\mu$ W).

in real space. From the separation  $\Delta Q_t$  between consecutive maxima along a truncation rod, the distance  $T$  along a pair of opposite side facets can be evaluated using

$$T = \frac{2\pi}{\Delta Q_t} \quad (1)$$

From the orientations  $\phi_1$ ,  $\phi_2$ , and  $\phi_3$  (see Figure 3 and 4) of neighboring truncation rods in reciprocal space, one is able to calculate the angle between neighboring side facets in real space. Furthermore, comparing  $\Delta Q_t$  measured along the three different truncation rods, one is able to calculate the thickness along all three opposing side facets marked by black, pink, and green in Figure 3 and 4. Because the thickness oscillations after application of current are still visible, the possible increase in interface roughness is negligible. This makes it possible to reconstruct the entire cross section of the investigated NW.

Based on the procedure mentioned earlier, we extracted the entire cross sections of the four investigated NWs as shown in Figure 4. Before conductivity measurements, all four NWs show almost hexagonal symmetry defined by equal thickness between opposite facets and equal angles between neighboring facets. After electrical treatment, we observe deformations of the hexagonal symmetry of the NW cross sections depending on the applied current. The thickness between each couple of opposing side facets is extracted for each of the investigated NWs, before and after electrical contact. The values of NW thickness are listed in Table 1. For NW A, where the lowest electrical current was applied, minor changes in about 5 nm were calculated for each pair of opposite side facet but the angles between the side facets stay all close to 60° as before the electrical impact. For NW B and NW C, we observe compression of NW thickness of about 40 and 20 nm, respectively, along the opposing side facet marked by a pink arrow. This was faced by the elongation of the other two opposing side facets marked by black and green arrows (see Figure 4, NW A before electrical contact for indication of the different side facets). For NW B and C, the angles between side facets did change by  $\pm 3^\circ$ – $5^\circ$ . For NW D, the deformation of the

**Table 1.** The NW thickness between opposing side facets before and after electrical treatment. Due to high deformation of its diffraction pattern, the thickness of NW D could not be evaluated.

Before electrical contact				
	NW A	NW B	NW C	NW D
Pink [nm]	226 ± 20	243 ± 19	222 ± 10	239 ± 18
Black [nm]	214 ± 17	239 ± 15	212 ± 12	262 ± 12
Green [nm]	204 ± 10	226 ± 18	203 ± 12	262 ± 10
After electrical contact				
Pink [nm]	221 ± 23	201 ± 40	200 ± 40	
Black [nm]	209 ± 15	280 ± 23	309 ± 40	
Green [nm]	200 ± 16	262 ± 31	242 ± 12	

RSM is so large, in particular the truncation rods disappeared completely after applying the highest electrical current, that it was not possible to reconstruct its cross section. This documents that NW D has the highest changes in its morphology compared to the other NWs. In contrast, no significant changes in length of all probed NWs have been observed.

### 3.3. SEM Characterization

To give evidence to our interpretation of the morphological changes extracted from the RSMs, SEM characterization was conducted on the same NWs. SEM microscopy images of NWs A–D are shown in Figure 5. To access the hexagonal cross section of each NW, the droplet-like feature at the NW top had to be removed. This feature results from the consumption of the Ga droplet at the end of the NW core growth process and exhibits a round shape which blocks access to the correct NW cross section. Therefore, prior to the SEM characterization experiment, almost 1.5  $\mu$ m of the NW length from top was removed by the FIB. To

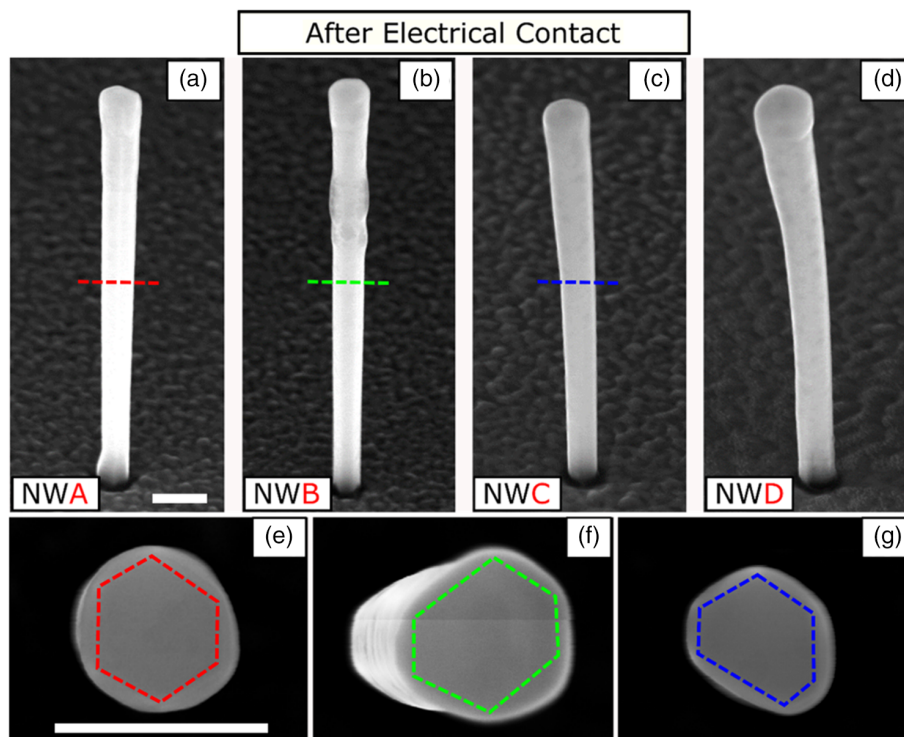


**Figure 5.** a–d) Tilted view SEM images of the investigated NWs and e–g) top view of corresponding NWs after cutting the NW by the FIB (scale bar is 500 nm).

avoid false estimations of the NW cross section, caused by NW being tilted or bended, we visualized the NW by top-view geometry. The positions along growth axes of NWs (A–C), at which the cross sections are inspected, are marked by dotted lines in Figure 5a–c whereas the estimated cross sections are indicated by dotted deformed hexagons in Figure 5e–g. The NW cross sections estimated from SEM confirm the results of nXRD. Both display the morphological changes caused by applied current such that: 1) the thickness between different opposing side facets changed significantly and 2) the hexagonal symmetry of the NW cross section is lost, except for NWA. Note that each of the NW cross sections estimated from the RSMs is an average of the NW volume illuminated by the incident X-ray beam. This can explain differences between NW cross sections reconstructed from the RSMs and estimated by SEM. In addition, the position at which the cross section is inspected by SEM can be different from the one illuminated during the nXRD experiment.

#### 4. Discussion

Since the RSMs obtained by nXRD before conductivity measurements (1st phase) reflect the nearly perfect hexagonal symmetry of the NWs' cross sections (see Figure 3 top row), the shape analysis by SEM and the nXRD experiment of the 3rd phase proves the morphological changes in the NWs as function of the electrical current density. For electrical current densities below  $30 \text{ A mm}^{-2}$ , the induced changes to the cross section of NW A are negligible whereas for a current density of  $347 \text{ A mm}^{-2}$ ,

the complete damage of the diffraction pattern was observed for NW D (see Figure 3). It should be mentioned that higher current densities of up to  $6 \text{ kA mm}^{-2}$  have been observed before by  $I$ – $V$  characterization of single InAs NWs in as-grown geometry<sup>[10]</sup>; however, the resistance of those NWs was two to three orders of magnitude lower than in the case of the GaAs NWs investigated here. Furthermore, the diameters of NWs B and C elongate along two directions and shrink along the third upon applying a current density of 55 and  $138 \text{ A mm}^{-2}$ , respectively. The morphological changes observed here can be explained by processes similar to liquid phase epitaxy<sup>[32]</sup> which considers local melting, material transport, and recrystallization. In fact, significant heating of the NW up to melting temperature is supposed because of Joule's heating during the electrical contact. Heat transport along the NW has been shown to occur extremely fast, in the order of a few ns, reaching an equilibrium between heat generated in the NW and heat conduction to the growth substrate as well as heat loss via the NW surface and convection in air.<sup>[12]</sup> Since both the volume of the NWs ( $0.1$ – $0.2 \mu\text{m}^3$ ) and their density ( $0.01 \mu\text{m}^{-2}$ ) are very low, the substrate can be considered as an almost infinite heat sink. Therefore, the electrical measurements can be considered to be performed under thermal equilibrium, and the time duration of the current flow through the NW is of negligible influence. However, even if one considers homogeneous heat distribution within the NW, the observed changes in the morphology must be explained by local inhomogeneity of material transport and recrystallization. The latter may be caused by phenomena such as inhomogeneity in strain distribution due to W-probe impact or the inhomogeneous

distribution of dopants in the NW bulk and oxide layer on the NW side planes.

Based on finite element method (FEM), one can estimate the temperature changes together with total heat flux magnitude depending on the electrical resistance of the GaAs NWs upon electrical treatment. For FEM simulations, we have considered a NW in its as-grown geometry, i.e., a homogeneous hexagonal cross section. The electric bias is applied between the NW top end and the substrate, resulting in current flow through the NW along its growth axis. Current pathways throughout the NW side planes are excluded. The impact of electrical current on the temperature is mediated by convective heat flux through the NW. The simulation was solved numerically by COMSOL Multiphysics which signifies electromagnetic losses as function of resistive losses. Figure S3, Supporting Information, shows changes in temperature and the total heat flux along the growth axis as a function of electrical resistance after applying an electrical current density of  $347 \text{ A mm}^{-2}$ . From the measured  $I$ - $V$  characteristics in the as-grown geometry of the NWs used in this experiment, one would obtain the electrical resistance of individual NWs to range from 200 kOhm to 2.5 MOhm, if one neglects interface barriers and other local sources of resistance. These values refer to a temperature within the NW ranging from 340 to  $910 \text{ }^\circ\text{C}$ , and a total heat flux ranging from  $0.12$  to  $1.53 \text{ kW mm}^{-2}$ . Such temperatures would result in a total destruction of some of the NWs, which is obviously not the case, thus the ohmic resistance of the NWs cannot exceed values of about 1 MOhm, and part of the measured resistance must be due non-ohmic effects such as interface barriers. Still, this simple evaluation shows that Joule heating of the NWs up to temperatures that result in local melting can be expected. It should be noted that the GaAs oxide layer on the NW surfaces is expected to cause surface band bending, resulting in a depletion layer close to the surface,<sup>[33,34]</sup> thus effectively decreasing the diameter of the conductive NW core and increasing the current density and therewith the effect of Joule heating in this conductive core. However, due to the high doping level of the NWs, the depletion layer is considered to be thin with respect to the relatively large NW diameter. Future work will focus more specifically on the role of the surface oxide on NW conductivity. Furthermore, the FEM calculation did not consider the existence of defects (dopants) in the NW bulk and possible inhomogeneity in the thickness of the surface oxide layer. However, even if the resistance may vary locally, the temperature will equalize rather fast across the NW cross section.<sup>[12]</sup> Therefore, inhomogeneous material transport and recrystallization is supposed to be the main reason for changes in morphology where possible inhomogeneity of dopant and defect distribution within the NW and the inhomogeneity of the oxide shell covering the NW side planes may cause local differences in strain. Moreover, inhomogeneous macroscopic strain is induced by the large W-probe during the electrical treatment. Approaching the probe onto the NW top surface induces compressive strain along the NW growth axis. Due to the Poisson effect, this axial strain is accompanied by tensile strain toward the NW side planes. Finally, this macroscopic strain field overlays with the local strain fields of defects (dopants) in bulk and below the surfaces which may experience strain-induced redistribution. Although detailed numerical simulation is missing, we argue that all fact together mentioned earlier may cause a scenario

of inhomogeneous migration of atomic species along defect channels toward the surfaces of NW side planes activated by Joule heating. Recrystallization takes place straight after switching off the current and takes place at those positions at the surfaces with maximum material that has migrated from molten bulk toward the surface where the different amount of migrating atoms is originated by inhomogeneous strain distribution. To explain the existence of oxide onto the side planes, it was discovered recently that the X-ray nanobeam causes oxide formation along the surface if the experiment has been performed in air.<sup>[18]</sup> Additional material also may come from carbon deposition during SEM. However, oxide formation and carbon deposition onto the side planes cannot explain the finding that the NW cross section deduced from nXRD after electrical impact seems to be larger compared to the as-grown state (see NW B and NW C). Since nXRD pattern is originated from the crystalline part of the material only, we suppose that the additional GaAs material stems from regions which were not illuminated by the X-ray beam.

## 5. Conclusion

We described the impact of electrical current on the structure of single Be-doped GaAs NWs. Comparing 2D X-ray diffraction patterns of the 111 Bragg reflection before and after application of electrical currents shows deformation of the hexagonal NW cross-section, in addition to tilting and bending. These structural deformations change as a function of applied electrical current density. We expressed our results by material diffusion induced by Joule heating along channels of local strain originated by defects (dopants) accompanied by local inhomogeneous recrystallization caused by inhomogeneity of oxide covering.

## Supporting Information

Supporting Information is available from the Wiley Online Library or from the author.

## Acknowledgements

Part of this work was performed at the Micro and Nanoanalytics Facility (MNaF) of the University of Siegen. This work was supported by DFG Pi217/38, DFG Pi217/46, BMBF (projects 05K16PSA and MILAS), and by the Swedish Research Council.

Open access funding enabled and organized by Projekt DEAL.

## Conflict of Interest

The authors declare no conflict of interest.

## Data Availability Statement

The data that support the findings of this study are available from the corresponding author upon reasonable request.

## Keywords

electrical characterization, semiconductor nanowires, structure–property relations, X-ray nanodiffraction

Received: February 9, 2021

Revised: May 5, 2021

Published online: May 29, 2021

- [1] A. G. Milnes, A. Y. Polyakov, *Mater. Sci. Eng. B* **1993**, *18*, 237.
- [2] P. Krogstrup, H. I. Jørgensen, M. Heiss, O. Demichel, J. V. Holm, M. Aagesen, J. Nygard, A. Fontcuberta i Morral, *Nat. Photonics* **2013**, *7*, 306.
- [3] K. Tomioka, M. Yoshimura, T. Fukui, *Nature* **2012**, *488*, 189.
- [4] X. Duan, Y. Huang, R. Agarwal, C. M. Lieber, *Nature* **2003**, *421*, 241.
- [5] R. Yan, D. Gargas, P. Yang, *Nat. Photonics* **2009**, *3*, 569.
- [6] W. Guo, M. Zhang, A. Banerjee, P. Bhattacharya, *Nano Lett.* **2010**, *10*, 3355.
- [7] L. Balaghi, G. Bussone, R. Grifone, R. Hübner, J. Grenzer, M. Ghobrani-Asl, A. V. Krasheninnikov, H. Schneider, M. Helm, E. Dimakis, *Nat. Commun.* **2019**, *10*, 2793.
- [8] J. Lähnemann, M. Hill, J. Herranz, O. Marquardt, G. Gao, A. AlHassan, A. Davtyan, S. Hruszkewycz, M. V. Holt, C. Huang, I. Calvo-Almazán, U. Jahn, U. Pietsch, L. J. Lauhon, L. Geelhaar, *Nano Lett.* **2019**, *19*, 4448.
- [9] G. Bussone, H. Schäfer-Eberwein, E. Dimakis, A. Biermanns, D. Carbone, A. Tahraoui, L. Geelhaar, P. H. Bolívar, T. U. Schüllli, U. Pietsch, *Nano Lett.* **2015**, *15*, 981.
- [10] R. Timm, O. Persson, D. Engberg, A. Fian, J. Webb, J. Wallentin, A. Jönsson, M. Borgström, L. Samuelson, A. Mikkelsen, *Nano Lett.* **2013**, *13*, 5182.
- [11] S. A. Dayeh, D. Susac, K. L. Kavanagh, E. T. Yu, D. Wang, *Nano Lett.* **2008**, *8*, 3114.
- [12] H. Wallander, J. Wallentin, *J. Synchrotron Radiat.* **2017**, *24*, 925.
- [13] M. A. Verheijen, R. E. Algra, M. T. Borgström, G. Immink, E. Sourty, W. J. P. van Enckevort, E. Vlieg, E. P. A. M. Bakkers, *Nano Lett.* **2007**, *7*, 3051.
- [14] H. Kauko, T. Grieb, R. Bjørge, M. Schowalter, A. M. Munshi, H. Weman, A. Rosenauer, A. T. J. van Helvoort, *Micron* **2013**, *44*, 254.
- [15] Z. Zhang, Y. Zhao, L. Sun, D. Liu, J. Shen, W. Zhou, Q. Luo, A. Jin, H. Yang, C. Gu, S. Xie, *J. Nanosci. Nanotechnol.* **2009**, *9*, 1119.
- [16] A. AlHassan, A. Davtyan, H. Küpers, R. B. Lewis, D. Bahrami, F. Bertram, G. Bussone, C. Richter, L. Geelhaar, U. Pietsch, *J. Appl. Crystallogr.* **2018**, *51*, 1387.
- [17] A. Davtyan, V. Favre-Nicolin, R. B. Lewis, H. Küpers, L. Geelhaar, D. Kriegner, D. Bahrami, A. AlHassan, G. Chahine, O. Loffeld, U. Pietsch, *MRS Adv.* **2018**, *3*, 1.
- [18] A. AlHassan, J. Lähnemann, A. Davtyan, M. Al-Humaidi, J. Herranz, D. Bahrami, T. Anjum, F. Bertram, A. Bikash Dey, L. Geelhaar, U. Pietsch, *J. Synchrotron Radiat.* **2020**, *27*, 1200.
- [19] C. Thelander, P. Caroff, S. Plissard, A. W. Dey, K. A. Dick, *Nano Lett.* **2011**, *11*, 2424.
- [20] S. N. Das, J.-H. Choi, J. P. Kar, K.-J. Moon, T. I. Lee, J.-M. Myounga, *Appl. Phys. Lett.* **2010**, *96*, 092111.
- [21] O. Wunnicke, *Appl. Phys. Lett.* **2006**, *89*, 083102.
- [22] D. R. Khanal, J. Wu, *Nano Lett.* **2007**, *7*, 2778.
- [23] F. Léonard, A. A. Talin, *Nat. Nanotechnol.* **2011**, *6*, 773.
- [24] H. Park, R. Beresford, R. Ha, H.-J. Choi, H. Shin, J. Xu, *Nanotechnology* **2012**, *23*, 245201.
- [25] F. Léonard, A. A. Talin, B. S. Swartzentruber, S. T. Picraux, *Phys. Rev. Lett.* **2009**, *102*, 106805.
- [26] A. A. Talin, F. Léonard, A. M. Katzenmeyer, B. S. Swartzentruber, S. T. Picraux, M. E. Toimil-Molares, J. G. Cederberg, X. Wang, S. D. Hersee, A. Rishinaramangalum, *Semicond. Sci. Technol.* **2010**, *25*, 024015.
- [27] A. M. Katzenmeyer, F. Léonard, A. A. Talin, P.-S. Wong, D. L. Huffaker, *Nano Lett.* **2010**, *10*, 4935.
- [28] C. Colombo, D. Spirkoska, M. Frimmer, G. Abstreiter, A. Fontcuberta i Morral, *Phys. Rev. B* **2008**, *77*, 155326.
- [29] H. Küpers, R. B. Lewis, A. Tahraoui, M. Matalla, O. Krüger, F. Bastiman, H. Riechert, L. Geelhaar, *Nano Res.* **2018**, *11*, 2885.
- [30] G. A. Chahine, M.-I. Richard, R. A. Homs-Regojo, T. N. Tran-Caliste, D. Carbone, V. L. R. Jacques, R. Grifone, P. Boesecke, J. Katzer, I. Costina, H. Djazouli, T. Schroeder, T. Schüllli, *J. Appl. Crystallogr.* **2014**, *47*, 762.
- [31] V. Holy, T. Baumbach, U. Pietsch, *High-Resolution X-Ray Scattering from Thin Films and Multilayers*, Springer, Berlin/New York **1999**, Chapter 8.
- [32] P. Capper, S. Irvine, T. Joyce, in *Springer Handbook of Electronic and Photonic Materials* (Eds: S. Kasap, P. Capper), Springer Handbooks, Springer, Cham **2017**.
- [33] M. Hjort, J. Wallentin, R. Timm, A. A. Zakharov, U. Håkanson, J. N. Andersen, E. Lundgren, L. Samuelson, M. T. Borgström, A. Mikkelsen, *ACS Nano* **2012**, *6*, 9679.
- [34] B. Khanbabaee, G. Bussone, J. V. Knutsson, I. Geijselaers, C. E. Pryor, T. Rieger, N. Demarina, D. Grützmacher, M. I. Lepsa, R. Timm, U. Pietsch, *J. Appl. Phys.* **2016**, *120*, 145703.